AIAA JOURNAL
Vol. 41, No. 6, June 2003

Stochastic Inlet Conditions for Large-Eddy Simulation of a Fully Turbulent Jet

David J. Glaze* and Steven H. Frankel†
Purdue University, West Lafayette, Indiana 47907-2014

A numerical study using the large-eddy simulation technique is performed to compare the behaviors of two different stochastic inlet condition methodologies, which are each intended to simulate a turbulent inflow for a round jet. The simple technique of Gaussian random forcing is tested as a baseline, and a version of the weighted amplitude wave superposition spectral representation method is tested as an improved technique. The Gaussian random inlet fluctuations were found to dissipate almost immediately, whereas the spectral inlet fluctuations were found to generate self-sustaining turbulence in the near field. Quantitative comparisons to experimental data revealed an unexpectedly strong coupling between the jet solution and the upstream pipe, which underscores the importance of proper inlet treatment for numerical simulations.

Introduction

CONTINUAL advances in computational hardware have made large-eddy simulation (LES) much more practical in recent years as a research tool for studying canonical turbulent flows at moderate Reynolds numbers. LES as a day-to-day engineering tool, however, is still beyond reach. High Reynolds numbers, complex physical geometries, and even chemical kinetics and multiphase flows must be easily simulated before LES can reach the same utility as Reynolds averaged Navier–Stokes (RANS) simulations for engineering use.

Although great progress is being made on all of these fronts, a fundamental problem still remains: turbulent inlet conditions. Obvious cost and complexity restrictions force researchers to focus their efforts on small sections of engineering systems, for example, a valve rather than an entire piping system or a combustor rather than an entire gas turbine engine. When the scope of a simulation is limited, some control over the boundary conditions is lost. It may be necessary to simulate a turbulent flow entering one or more computational domain boundaries.

Depending on the closure model chosen for RANS simulations, it may only be necessary to impose parameters such as turbulent kinetic energy and dissipation rate on a turbulent inflow. Although this is not without its challenges, it is certainly easier to specify characteristics of a turbulent flow than it is to generate the turbulence itself. The latter is, unfortunately, necessary for time-resolved simulation techniques such as LES and direct numerical simulation (DNS).

In the literature to date, a vast majority of the nonperiodic DNS or LES studies have been of transitional turbulent flows presumably because the inlet conditions are clearly defined and straightforward to implement.[1–4] Harmonic forcing with superimposed random velocity fluctuations is commonly used to supply the necessary excitation frequencies to initiate shear layer instability and an eventual transition to turbulence. When it becomes necessary to simulate a complex fully turbulent flow, however, this type of treatment is no longer appropriate. Because both experimental and numerical measurements indicate a strong sensitivity to inlet conditions,[5–8] their correct specification is critical.

Many different approaches have been developed to approximate a turbulent inflow. One very successful class of techniques can be though of as deterministic, where data are extracted directly from a numerical simulation or experimental measurement. Periodic boundary conditions, for instance, can work very well for simple configurations such as temporally developing shear layers or fully developed turbulent pipe or channel flows.[9] Its use in spatially developing flows, however, is limited to only very simple configurations that obey known scaling laws.[10] In many special circumstances, turbulent inlet conditions can be extracted directly from the results of an auxiliary simulation, for example, pipe flow for a turbulent jet simulation.[11–13] In what is commonly referred to as the temporal method, a complete time series is extracted from a stationary plane in the auxiliary simulation. This may, however, lead to problems with the storage and handling of vast quantities of data. In what is commonly called the spatial method, data are gathered from a plane that is repeatedly swept through a block of the auxiliary solution. In this case, breaking up periodicity becomes an issue.[14] Semideterministic forcing techniques are also possible, which supplement limited measurements with modeled turbulent fluctuations.[15] In general, though, deterministic approaches are not always practical or possible with arbitrarily complex flow configurations and, thus, have limited applicability as an engineering tool.

For fully turbulent flows, it would ideally be possible to synthetically generate realistic turbulent inlet fluctuations without the expense or complexity of an auxiliary simulation. Unfortunately, the complex and chaotic physical structure of turbulence does not lend itself well to this type of modeling. Turbulence, by its nature, is governed by the Navier–Stokes equations. Generation of realistic turbulent fluctuations independently of these equations is a challenging proposition.

There is, however, a large class of techniques available for simulating correlated stochastic fields that has met with good success in the area of structural analysis, where it is often necessary to simulate physical loadings due to atmospheric turbulence, ocean waves, or even earthquakes. The simplest stochastic technique is to use just a random signal with a desired probability distribution.[16] A more advanced approach is to use a version of the autoregressive moving-average method.[17–19] Although this class of techniques is very powerful and computationally efficient, determining the model coefficients can be challenging, stability issues may arise, and it is not possible to simulate nonhomogeneous spatial fields. A more robust class of techniques includes versions of the constant amplitude wave superposition spectral representation method[20] and the weighted amplitude wave superposition (WAWS) spectral representation method.[21–23] Despite possibly being costly,[24] these techniques

Presented as Paper 2001-2548 at the AIAA 15th Computational Fluid Dynamics Conference, Anaheim, CA, 11–14 June 2001; received 5 June 2002; revision received 15 January 2003; accepted for publication 15 January 2003.

*Ph.D. Candidate, Department of Mechanical Engineering. Student Member AIAA.

†Associate Professor, Maurice J. Zucrow Laboratories, Department of Mechanical Engineering, 500 Allison Road; frankel@purdue.edu. Senior Member AIAA.

are capable of easily simulating multivariate, multidimensional, nonhomogeneous stochastic fields with evolutionary power spectra and arbitrary probability distributions.[22,25–27]

Although versions of some of these stochastic techniques have been used in the context of turbulent inlet conditions,[28,29] their general suitability has not yet been fully characterized. Pure random fluctuations are obviously deficient for describing turbulent flows, yet it has still made its way into several commercial computational fluid dynamics (CFD) codes. It is suspected that nearly any inlet condition methodology that correctly captures the spatial and temporal correlation of a real turbulent flow will provide better simulation results than uncorrelated white noise. To test this hypothesis, the present work will assess two stochastic inlet condition techniques for use in LES. Gaussian random fluctuations will be tested as a baseline, and a version of the WAWS spectral representation method will be tested as an improved technique. By comparison with the experimental data of Amielh et al.[30] and Djeridane et al.[31] for a fully turbulent jet, the usefulness of these two stochastic turbulent inlet conditions will be assessed.

Computational Approach

Numerical Methodology

The LES governing equations used in this study are the standard Favre-filtered compressible Navier–Stokes, energy, and mixture fraction equations.[32] A sixth-order compact finite difference spatial discretization scheme is used,[33] which ensures little contamination of the high wave number components of the solution that are heavily relied on by most LES subgrid-scale (SGS) closure models.[34,35] A fifth-order compact scheme is used for the two grid points nearest the boundary.[36] The lower order of the boundary-adjacent point reduces the formal accuracy of the overall method to fifth order, which is a tradeoff made to ensure the time stability of the overall compact differencing scheme. Time advancement of the solution is achieved with a standard fourth-order Runge–Kutta method.

Most high-order compact finite difference schemes are known to not be energy conservative when physical boundary conditions are imposed on a solution, leading to a long-time instability.[37] To remedy this, a sixth-order compact pentadiagonal low-pass filter is applied to the entire solution at each time step to remove the destabilizing high wave number noise.[33] This also serves as an explicit grid filter, rather than relying on the finite support of the computational mesh.

SGS Turbulence Models

Dynamic SGS closures based on the Smagorinsky eddy-viscosity model have become quite popular because of their simplicity and their reasonably good performance when applied to a variety of different flow configurations (see Ref. 38). When the Germano identity[39] is used, the dynamic model coefficient can be calculated in terms of the smallest flow structures remaining after two different levels of filtering: the grid-level filter and a larger test filter. A rigorously derived model within this class has been proposed by Ghosal et al.,[40] which requires solving an integral equation for the model coefficients. This can be quite cost prohibitive, and so it is common practice to assume a small spatial variability of the model coefficient that greatly simplifies the problem by not requiring a solution of these integral equations.[41] As a consequence of this assumption, inconsistencies in the model can sometimes lead to large fluctuations in the calculated model coefficients, causing nonphysical results and even numerical instability. These fluctuations are usually controlled by some form of an averaging operation, either in a statistically homogeneous direction or over an ad hoc local volume. In the present work, averaging is done over fluid pathlines by using the Lagrangian dynamic SGS closure model of Meneveau et al.[42] Fluid pathlines are the natural frame of reference for the development of turbulent eddies, yielding a consistent direction for averaging the effects of localized flow structures.

Inlet and Boundary Conditions

Physical boundary conditions are implemented using the characteristic-based approach of Poinsot and Lele.[43] The inlet and boundary conditions are configured to simulate a fully turbulent round air jet at a Reynolds number of 2.1×10^4 based on the jet diameter D and centerline velocity U_j. A weak coflow of 1/12th the centerline velocity surrounds the jet, and the mixture is exhausted into a large, square duct to provide weak flow confinement. These simulation conditions are chosen to match the experimental setup of Amielh et al.[30] and Djeridane et al.[31] at the Institut de Recherche sur les Phénomènes Hors Equilibre (IRPHE), who performed detailed near-field measurements of several first-, second-, and third-order turbulence statistics in variable-density jets.

To match the experiment, the duct walls are placed $5.48D$ from the jet centerline. The simulation domain extends $20D$ downstream to encompass the experimental measurement region, and an additional numerical buffer zone of length $10D$ is added to the downstream boundary. The buffer zone uses axial grid stretching and an artificial increase in fluid viscosity to damp any nonphysical acoustic reflections from the downstream open boundary condition. Simulation results from within the buffer zone are discarded.

The inlet to the computational domain is chosen to correspond to a plane $0.2D$ downstream of the jet nozzle simply because this is the farthest upstream location that data are available from the IRPHE measurements. Inlet conditions are specified by imposing a mean velocity profile on the flow with superimposed stochastic fluctuations that are intended to simulate the turbulence. The computational domain placement and inlet condition profiles are shown schematically in Fig. 1. Nondimensional parameters are used in Fig. 1 and subsequently, with the mean axial velocity defined as $U^* = (U - U_{co})/(U_j - U_{co})$ and the axial turbulence intensity defined as $(u')^* = u'/(U_j - U_{co})$, where U is the local mean velocity, U_j is the jet nozzle centerline velocity, and U_{co} is the uniform coflow velocity. The radial and azimuthal mean velocity components are negligible at this axial location of $x/D = 0.2$ and are specified as zero in the simulation. The radial and azimuthal turbulence intensity components follow a qualitatively similar trend to the axial component, but are not shown in Fig. 1 for clarity. A sharp hyperbolic tangent profile is chosen for the mixture fraction Z because little mixing will have occurred at this axial location.

Two different techniques are used to model the inlet turbulence: Gaussian random fluctuations and a version of the WAWS spectral representation method originally formulated by Shinozuka and Jan.[21] In the Gaussian random technique, the fluctuation values for

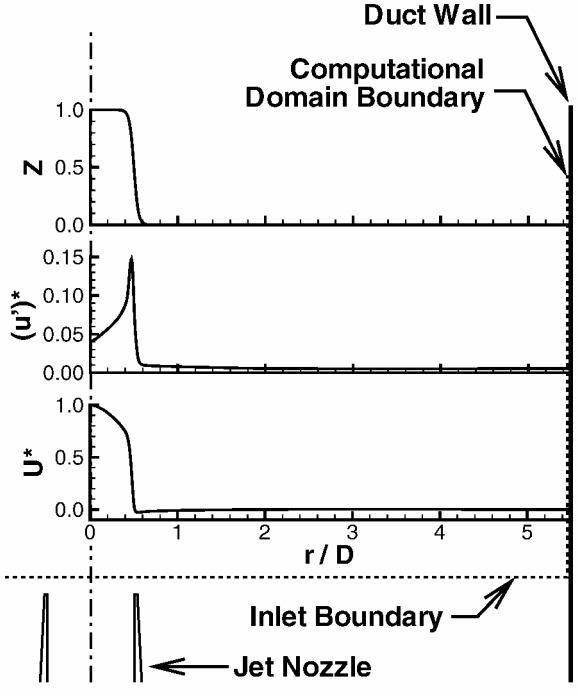

Fig. 1 Computational domain configuration and inlet condition profiles for LES.

all three velocity components are sampled from a Gaussian probability density function at each time step. The intensity is scaled everywhere across the inlet plane to match the experimental measurements. Because of the random nature of this inlet forcing, no spatial or temporal correlation is possible.

Conversely, the WAWS spectral representation method is capable of simulating both spatial and temporal correlation. This is done through a careful reconstruction of a fluctuation signal from its Fourier components, which are extracted from a modeled cross-spectral density across the inlet plane. The resulting signal varies smoothly in time and space and matches a target power spectrum and spatial correlation across the inlet plane. Although some researchers have been able to simulate Reynolds stresses with similar techniques,[29] no attempt is made here to model these higher-order statistics.

The spectral representation method begins by arbitrarily numbering each of the M grid point across the inlet plane, so that the time series for the fluctuation of a single velocity component for inlet grid point i can be simulated by

$$u_i(t) = \sqrt{2}\sum_{m=1}^{i}\sum_{n=1}^{N} |H_{im}(\omega_n)|\sqrt{2\Delta\omega}\cos[\omega'_n t + \theta_{im}(\omega_n) + \phi_{mn}] \tag{1}$$

This equation represents a summation over N frequencies, defined as

$$\omega_n = \left(n - \tfrac{1}{2}\right)\Delta\omega \tag{2}$$

$$\omega'_n = \omega_n + \delta\omega_n \tag{3}$$

where $\Delta\omega = \omega_u/N$ is the frequency spacing, ω_u is the upper cutoff frequency, and $\delta\omega_n$ is a small random perturbation distributed between $-\Delta\omega'/2$ and $\Delta\omega'/2$ to destroy periodicity in the generated fluctuations. To avoid any significant drift from the target power spectrum, $\Delta\omega'$ is given a value of $\Delta\omega/10$. The parameters ϕ_{mn} are a set of independent random phases uniformly distributed between 0 and 2π. For all simulations presented here, the upper cutoff frequency ω_u is fixed so that the simulated signal contains 85% of the target power. Because the simulated frequencies are equally spaced, this ensures an adequate frequency resolution at the low wave number energy-containing portion of the spectrum, while neglecting contributions from the extreme highest wave numbers that would otherwise be filtered out of the LES solution.

The variables $H_{im}(\omega_n)$ in Eq. (1) are components of a transfer function matrix, defined in general as

$$\boldsymbol{S}(\omega_n) = \boldsymbol{H}(\omega_n)\boldsymbol{H}^H(\omega_n) \tag{4}$$

where superscript H represents a Hermitian transpose and $\boldsymbol{S}(\omega_n)$ is the cross-spectral density (CSD) matrix whose components $S_{im}(\omega_n)$ are defined as the Fourier transform of the cross correlation $R_{im}(\tau)$ between spatially separated points i and m across the inlet plane. The generally complex components $H_{im}(\omega_n)$ can be written in polar form as

$$H_{im}(\omega_n) = |H_{im}(\omega_n)|\exp[i\theta_{im}(\omega_n)] \tag{5}$$

which defines $\theta_{im}(\omega_n)$ in Eq. (1) as

$$\theta_{im}(\omega_n) = \tan^{-1}\left\{\frac{\mathrm{Im}[H_{im}(\omega_n)]}{\mathrm{Re}[H_{im}(\omega_n)]}\right\} \tag{6}$$

Note that the matrix $\boldsymbol{H}(\omega_n)$ is not unique for a given $\boldsymbol{S}(\omega_n)$ and can be calculated in a number of ways. Cholesky decomposition is used in the present work, which reduces $\boldsymbol{H}(\omega_n)$ to a lower-triangular matrix, greatly simplifying calculations.

All that is needed to use this simulation technique is the CSD matrix for each of the three velocity components. Unfortunately, detailed cross-spectral data are unavailable for the present flow, so that models must be used. The CSD between two spatially separated points is related to the two-sided autospectrum through the complex coherence function γ_{im} as[44]

$$S_{im}(\omega_n) = \gamma_{im}\sqrt{S_{ii}(\omega_n)S_{mm}(\omega_n)} \tag{7}$$

Very detailed empirical correlations exist for the coherence function for some turbulent flows, such as the atmospheric boundary layer. However, no known correlations or coherence data exist for the near-field of a turbulent jet. Thus, a modified version of a simple exponential-decay model[44] is used here:

$$\gamma_{im} = \exp\left\{-\left[A\left(r_{im} + Br_{im}^2\right)\omega_n / U_{im}\right]\right\} \tag{8}$$

where r_{im} is the distance between points i and m and U_{im} is the average mean velocity between the two points. All parameters in this expression have been nondimensionalized by the jet diameter and centerline velocity. The constants A and B are given values of 1 and 4, respectively, which are chosen to yield qualitatively realistic velocity fluctuations. The quadratic term was added to this model to limit the low-frequency correlation across large distances, which was observed to cause an unnatural large-magnitude oscillation in the mass flux through the inlet plane.

Detailed power spectra in the extreme near field of a fully turbulent jet at this Reynolds number are, to the authors' knowledge, not currently available in the open literature. Thus, a version of the von Kármán model spectrum is used (see Ref. 45):

$$S_{ii}(f) = \frac{4\tilde{f}(u')^2}{f(1 + 70.8\tilde{f}^2)^{\frac{5}{6}}} \tag{9}$$

which is parameterized in terms of the rms turbulence intensity u', the frequency f (in hertz), the integral length scale L_u, and the mean velocity U, where the nondimensional frequency is defined as $\tilde{f} = L_u f/U$. All parameters in this model spectrum are known at the inlet plane except for the integral length scale. To determine this parameter, spectra from Bremhorst and Walker[46] for pipe flow at a Reynolds number of 5.356×10^4 are scaled to the fluctuation intensities found in the present jet, and the model integral length scale is then specified to fit these data. All parameters for the coherence and power spectrum models vary spatially across the jet radius through the use of cubic spline curve fits to the known data.

Because both computational cost and storage for this technique are $\mathcal{O}(M^2)$, the number of simulated grid points and frequencies must be restricted to yield an affordable calculation. Turbulent structures inside the jet pipe will obviously be uncorrelated with structures in the coflow outside the pipe. Appreciable correlation between these two zones will not likely develop within the first 0.2 jet diameters downstream of the nozzle, which is where the inlet conditions are actually specified. As such, the inlet plane is broken into three zones that are simulated independently. The first zone covers the area immediately downstream of the jet nozzle and extends to a radius of $r/D = 0.55$. The second zone extends from this location through a radius of $r/D = 0.8$ to capture a majority of the external boundary layer. For reasons of cost, Gaussian random fluctuations are used outside $r/D = 0.8$ to match the low-freestream-turbulence level of the coflow. The inlet simulation uses 64 discrete frequencies in the jet and 32 frequencies in the external boundary layer for each of the three velocity components.

Grid and Parallel Computation Issues

The LES are performed on a $216 \times 120 \times 120$ Cartesian computational grid, with grid compression used near the jet nozzle to better resolve the shear layer. The grid is shown in Fig. 2 at one-third density, for clarity.

The present simulation would not be possible in a reasonable time frame without running in parallel. The message passing interface (MPI) was chosen as the interprocess-communication library because of its portability, allowing the code to run without modification on both shared-address space and distributed-address space supercomputers, as well as clusters of stand-alone workstations.

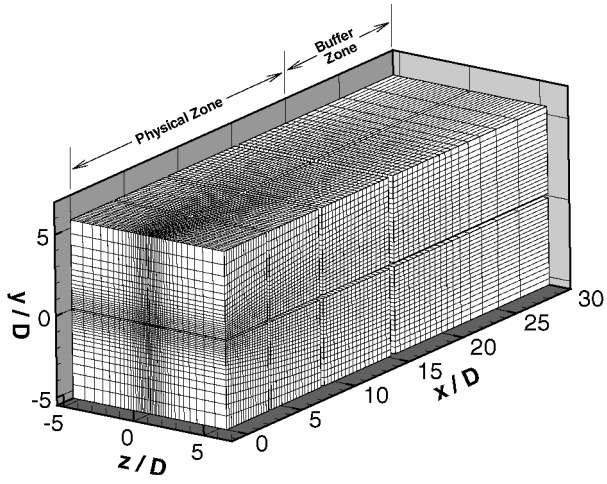

Fig. 2 Computational grid illustrating parallel domain decomposition (one-third density grid).

The physical domain is decomposed into 16 three-dimensional blocks, with each processor being responsible for a single block. The decomposition can be seen as gaps in the grid in Fig. 2. The spectral representation inlet condition methodology has a very natural parallel decomposition in frequency space. Each processor calculates the fluctuations from a small frequency range, and the final signal is simply a summation of these. The compact finite difference and compact filtering methodologies, however, require special treatment due to their semi-implicit nature. To resolve this issue, the parallel tridiagonal matrix algorithm developed by Mattor et al.[47] and an extension of this technique for pentadiagonal systems are used in the solution. Both of these techniques yield good parallel performance for the simulations presented in this study.

LES Numerical Accuracy

As mentioned, the solution is passed through a sixth-order compact grid filter for numerical stability reasons. Ideally, this filter would be several orders higher accuracy than the flow solver to avoid excessive contamination of the solution with truncation errors. Recall that two rows of grid points at each boundary are solved with a fifth-order method for stability. This reduces the formal accuracy of the overall numerical method to fifth order, and so there is only one order of separation between the filter and solver. Decreasing the order of the solver was undesirable because this would require more grid resolution to obtain an equivalent solution accuracy, which would increase memory and storage requirements to impractical levels. Increasing the order of the filter was also undesirable because this would have necessitated a larger right-hand-side or left-hand-side stencil. The additional cost, storage, and parallel communication overhead at the subdomain boundaries for this was also prohibitive.

As a concession, the spectral resolution of the filters was increased by solving a pentadiagonal system rather than a tridiagonal system, as was used for the flow solver. The pentadiagonal grid and test filter transfer functions are both shown in Fig. 3. The spectral cutoff of the grid filter is moved close to the maximum supported wave number on the grid. When the solution is grid filtered, a portion of the erroneous high-wave-number components of the solution is removed, as approximated by the shaded range of the modified wave number[33] in the lower portion of Fig. 3.

The solution dependence on grid resolution is shown in Fig. 4, where the centerline axial velocity is shown for a typical simulation using the Gaussian random inlet condition methodology. The functional form of the test filter used prevented filter sizes larger than that already used, and so grid refinement tests independent of the physical filter size were not performed. Alternatively, the same code configuration was run at three different resolutions: the final $216 \times 120 \times 120$ grid and two more that were roughly three-quarters and one-half of this resolution in each direction. The final

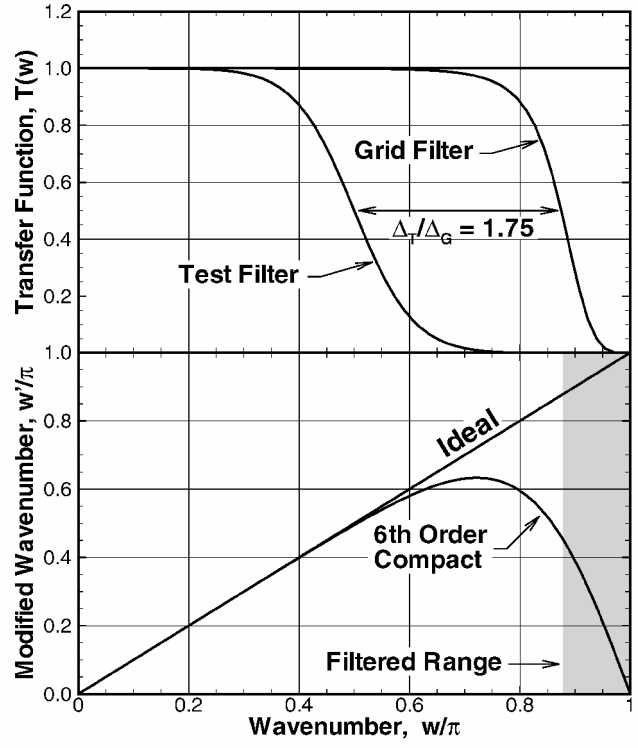

Fig. 3 Grid and test filter transfer functions and the solver modified wave number.

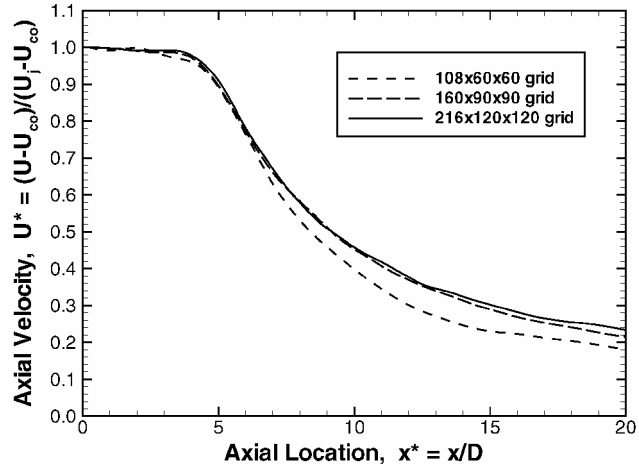

Fig. 4 Grid dependence of the jet centerline axial velocity.

and the three-quarter resolutions yielded nearly identical results, but the finer mesh was chosen to eliminate doubt about the solution accuracy.

Estimates indicate that the Kolmogorov length scales in the downstream portions of the jet are generally around 30 times smaller than the grid size, so that the smallest dissipative scales are certainly unresolved. Figure 5 confirms this by showing that the time-averaged subgrid stress dominates the resolved viscous stress at $x/D = 10$. Similar behavior is seen for the other components of the stress tensors and at other physical locations in the jet. Figure 6 shows an axial profile of the turbulence intensity, both with and without the SGS model activated. Without the model, the initial transition to turbulence occurs more rapidly, which slightly broadens the jet velocity profile and decreases the turbulence production rate. The centerline intensity peaks sooner, and the downstream development follows an almost identical trend.

The grid filter is needed for long-time stability of the simulation, but when both the grid filter and the SGS model are deactivated, the code destabilizes almost immediately. Because the code runs

stable with only the grid filter, this matches the recent observation that grid filters used with compact solvers can act as an SGS model themselves.[48] Efforts to quantify this effect are outside the scope of the present work and are not attempted.

Fluent Simulations

As will be discussed in the following sections, several RANS simulations were performed to complement the LES. For simplicity, the Fluent commercial CFD code was used. The axisymmetric domain geometry is illustrated schematically in Fig. 7, with notable features including an $80D$ length of the upstream jet pipe and a small section of the upstream duct.

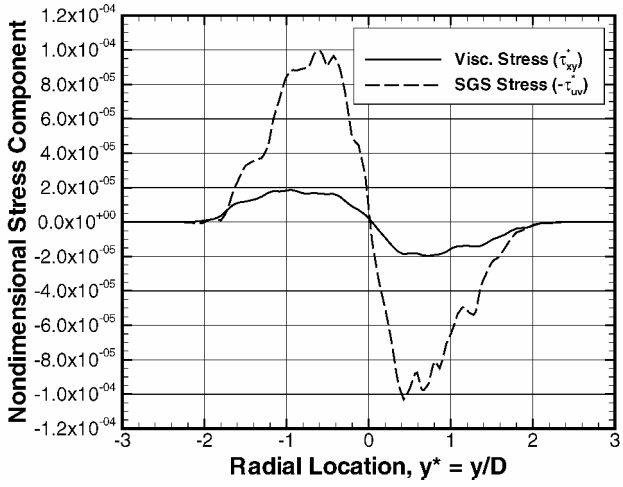

Fig. 5 Transverse profiles of a resolved viscous and SGS stress component at $x/D = 10$.

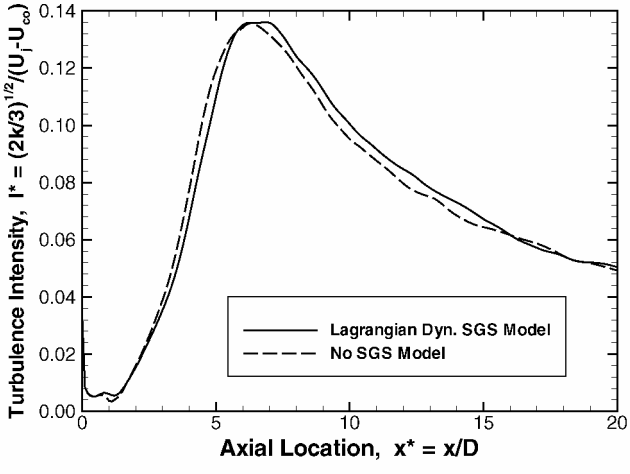

Fig. 6 Axial profile of turbulence intensity both with and without the SGS model.

This domain geometry was chosen to eliminate any possible effects on the flow caused by the inlet conditions, which would otherwise have been applied at $x/D = 0.2$ downstream of the jet nozzle. Because the correct inlet conditions for this expanded geometry are unknown, approximate velocity profiles were applied and then iteratively adjusted until the centerline velocity at $x/D = 0.2$ matched that of the experimental data. The long inlet pipe is used so that the pipe velocity profile obtains a fully developed state before the nozzle is reached.

Careful attention was paid to grid resolution in the RANS simulations, especially in the near-wall region of the pipe. A two-layer zonal model was used to treat the walls, and the first grid point is everywhere less than $y^+ = 0.5$ from the wall to ensure accuracy of this model. These RANS simulations contain 302,000 grid cells, with 251,000 used for the upstream pipe. To assess grid independence, adaptive mesh refinement was used in regions of large gradients of the major transport variables, bringing the grid count up to 436,000. No differences larger than 1% were found in the mean velocity field, indicating an essentially grid-independent solution without additional refinement.

In addition to the axisymmetric RANS simulations, a three-dimensional LES was performed with Fluent. To yield a more affordable calculation, the domain size was reduced from that used with the LES research code. The Fluent LES domain extends $12D$ in the axial direction, and the sidewalls are placed $3D$ from the centerline to assure no interaction with the jet other than weak confinement. A $140 \times 70 \times 70$ computational mesh with compression near the jet nozzle was used, which yielded near-field grid densities about 20% less than in the research LES and an overall qualitatively similar grid distribution. The unsteady second-order implicit temporal solver was used, with a second-order central differencing spatial discretization to eliminate implicit numerical dissipation. For subgrid closure, the renormalization group (RNG) dynamic model was used.

Mean profiles for the Fluent LES inlet conditions were taken from the experimental data at $x/D = 0.2$. Fluent uses Gaussian random perturbations to simulate inlet turbulence as in the baseline research LES code configuration, but a fixed relative intensity is required as an input. As an approximation of the range of values found across the jet profile, an intensity of 10% is used.

Results and Discussion

Inlet Condition Behavior

The fundamental difference between the inlet conditions used in the Gaussian random LES (GR LES) and the spectral representation LES (spectral LES) can be easily seen in Fig. 8. Here, typical instantaneous snapshots of axial velocity across the inlet plane are shown, with the magnitude inferred from the height of the surface. As one would expect from random fluctuations, the GR inlet profile has many sharp peaks and valleys that do not realistically characterize a fluid flow. Conversely, the spectral representation inlet velocity profile is much more representative of a turbulent fluid. Many different fluctuation length scales are visible, and they are all smoothly varying, within the obvious restrictions of grid resolution. The temporal variation of these two inlet methodologies is shown in Fig. 9 for the grid point on the jet centerline. The spectral fluctuations are reminiscent of an actual time series measured from a turbulent flow,[49]

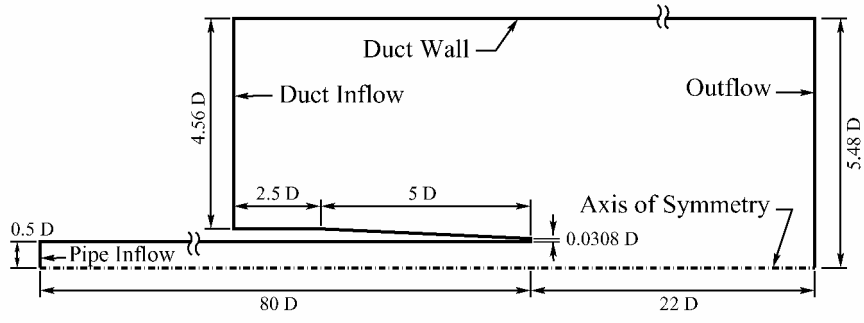

Fig. 7 Computational domain configuration for Fluent RANS simulations.

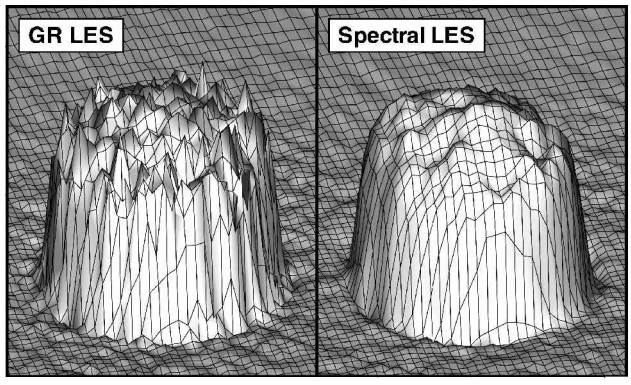

Fig. 8 Instantaneous snapshot of inlet velocity profiles.

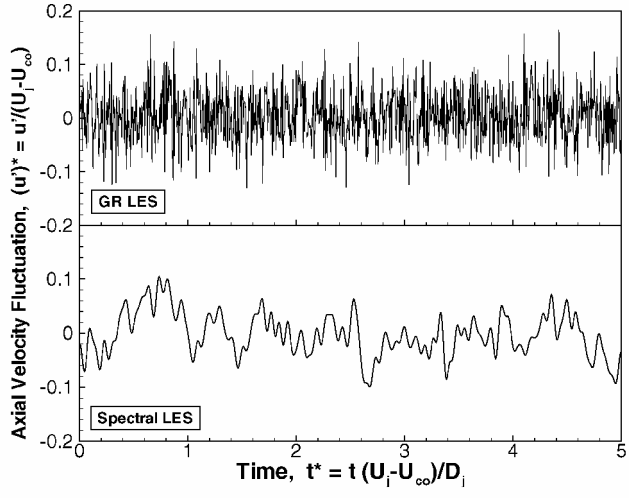

Fig. 9 Representative axial velocity time series for an inlet grid point on the jet centerline.

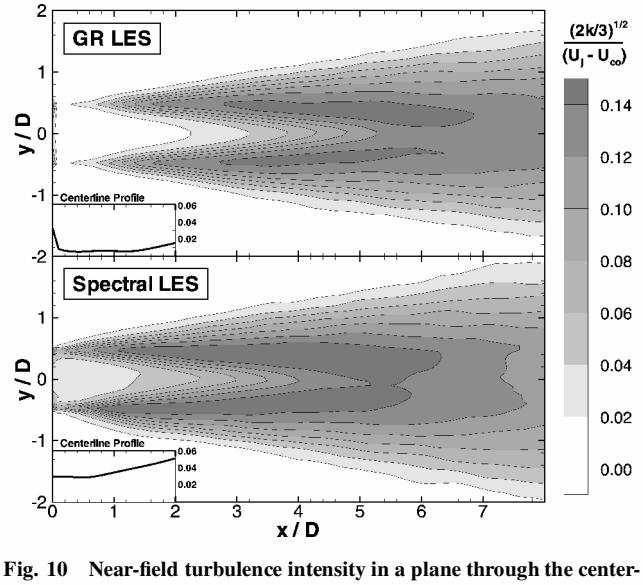

Fig. 10 Near-field turbulence intensity in a plane through the centerline of the jet.

whereas the random fluctuations are not. The GR fluctuations have no spatial or temporal correlation between any two inlet grid points or any two time levels, unlike in a real turbulent flow.

The way the near-field flow responds to these two inlet forcing schemes can be seen in the near-field average turbulence intensity, shown in Fig. 10. Both simulations are forced with the same turbulence intensity across the inlet plane; however, the response is significantly different. In the GR LES, the intensity at the inlet

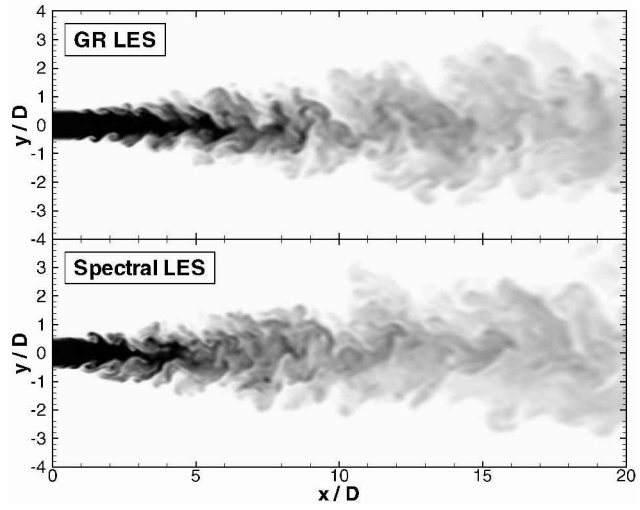

Fig. 11 Instantaneous mixture fraction in a plane through the centerline of the jet.

plane drops almost to zero as the random fluctuations are dissipated, similar to the observations of Branley and Jones.[50] The intensity remains close to zero until the merging shear layers bring the level back up. The spectral LES does not experience the same drop in turbulence levels. In fact, the turbulence levels at the inlet hold their value roughly constant for a short time before the growth begins. This is the correct near-field behavior for a jet that is fed by a fully turbulent pipe flow.[30]

The higher near-field turbulence levels in the spectral LES lead to enhanced mixing between the jet and the coflow. This can be seen qualitatively in Fig. 11, which is an illustration of the instantaneous mixture fraction in a plane through the centerline of the jet. Clearly, regions of unmixed jet fluid are present farther downstream in the GR LES. The mixing in the spectral LES begins sooner and is apparently more thorough, as evidenced by the wider downstream jet profile and independent observations of smaller mixture composition standard deviation.

Qualitative comparisons between the mixture fraction distribution in the spectral LES of Fig. 11 and equivalent images from an experimental fully turbulent jet by Mi et al.[6] reveal some differences. The spectral representation inlet conditions seem to possess an abundance of large-scale structure where the experimental image shows primarily small-scale structure. This difference is likely due to errors in the specification of the model coherence function and power spectrum. With proper data on which to base these models, it is presumed that this comparison would be closer. Despite this inconsistency, the spectral representation inlet condition methodology is capable of generating distinctly more realistic near-field turbulent structure than simple random fluctuations.

A clearer view of the near-field turbulence structure is visualized in Fig. 12 for both the GR and spectral LES, as well as a comparable LES performed with the Fluent commercial CFD code, as described earlier. Isosurfaces of negative second eigenvalues of the tensor $(S_{ik}S_{kj} + \Omega_{ik}\Omega_{kj})$ are plotted to isolate vortical structures in the flow, independent of the mean shear-generated vorticity.[51]

Although it is partially obscured in Fig. 12, there is almost no turbulent structure visible in the near-field core of the GR LES. Conversely, there is structure found throughout the near-field core of the spectral LES. Additionally, the GR LES is seen to possess intermittent Kelvin–Helmholtz-type instabilities in the shear layer that switch between forming discrete vortex rings and helical structures. The helical mode is visible in Fig. 12. Although more disorganized, the behavior of the GR LES is reminiscent of a transitional turbulent jet fed by a laminar inflow, where shear layer instability is the driver of the transition to turbulence. A qualitative change in the structure of this jet is visible about three jet diameters downstream of the nozzle, where a transition to turbulence is likely beginning.

No such transitional jet behavior is found in the near field of the spectral LES. Qualitatively, the disorganized turbulent structure is

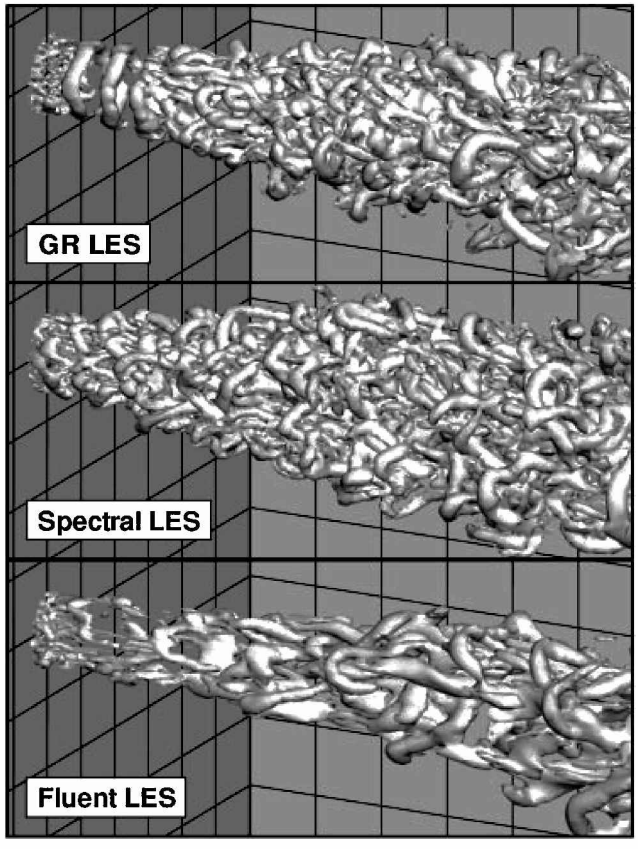

Fig. 12 Instantaneous vortical structures visualized by negative λ_2 isosurfaces.

consistent almost all of the way up to the jet nozzle. The spectral inlet fluctuations are generated independently of the Navier–Stokes equations and are, thus, just as nonphysical as the GR fluctuation. However, their coherent and smoothly varying nature appears to seed an almost immediate transition to real turbulence. This earlier transition contributes to the broader jet profile seen in Fig. 12.

The Fluent LES in Fig. 12 bears a strikingly different structure from either research-code LES. Because it also uses GR inlet fluctuations, the near field most closely resembles the GR LES. The core is almost absent of structure, and intermittent partial vortex rings in the shear layer are swept into horseshoe vortices that tangle together and eventually transition to turbulence far downstream. The transition is not as rapid as in the other two simulations, and the overall vortical structures are larger and more coherent. Although the grid is only slightly coarser than in either research LES, the numerical method is only second order in space and has a much lower spectral resolution.[33] This, coupled with a finite volume formulation of a different SGS closure model likely explains the differences. Despite the differences, several of the GR inlet condition traits are still visible.

To investigate further the difference between the transition behaviors of the GR and spectral LES, Fig. 13 shows the radial velocity power spectral density in the shear layer, measured at $x/D = 2$ and $y/D = 0.5$. The reference time used in the nondimensionalization of Fig. 13 is defined as $t_{\text{ref}} = D/(U_j - U_{\text{co}})$. The nontraditional linear axes for Fig. 13 are used to accentuate the lower-frequency components that are dominant during transition to turbulence. Although somewhat noisy, the curve for the GR LES increases to a broad peak centered at roughly $f^* = 0.7$, which is the most amplified frequency from the inlet forcing,[52] and then rapidly decreases toward larger frequencies. Qualitatively, this is the exact same trend as was found by Mi et al.[6] in an initially laminar transitional jet with a top-hat velocity profile. In the same work, a jet driven by a fully developed turbulent pipe flow showed a power spectrum that peaks at the lowest-frequency and monotonically decreases toward higher frequencies. The spectral LES power spectrum is somewhat closer to

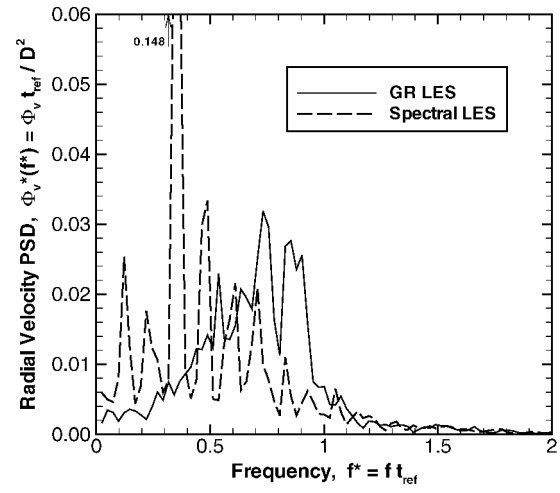

Fig. 13 Radial velocity power spectral densities measured at $x/D = 2$ in the center of the shear layer.

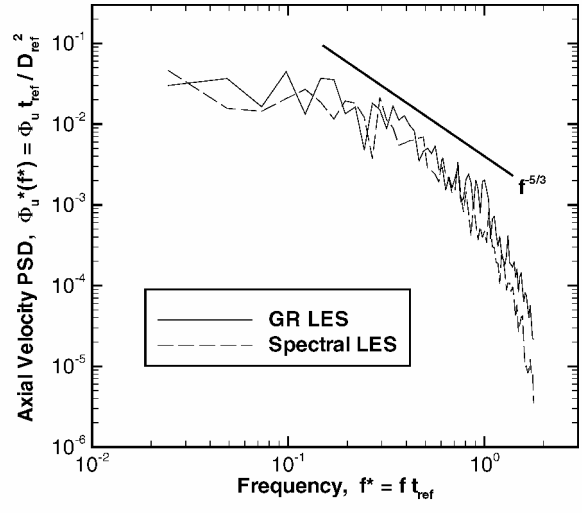

Fig. 14 Axial velocity power spectral density measured at $x/D = 10$ on the jet centerline.

this behavior, although the discrete forcing frequencies make interpretation of Fig. 13 challenging. The model power spectrum used in this simulation [Eq. (9)] possesses the characteristic of a monotonically decreasing magnitude, although the extreme lowest-frequency components of the inlet forcing were apparently not retained by the flow at this location.

An axial velocity power spectrum measured on the jet centerline at $x/D = 10$ is shown in Fig. 14. Although somewhat noisy due to the limited number of samples available, the energy cascade follows expected patterns for both simulations. The power spectrum for the spectral LES lies below the spectrum for the GR LES because the turbulent kinetic energy at this location is about 24% lower.

Comparison to Experimental Data

The GR LES and Spectral LES inlet conditions are both models of the the experiments performed at IRPHE.[30,31] In Fig. 15, radial profiles of mean axial velocity are compared with these experimental data. The profiles match exactly at $x/D = 0.2$ because this is the inlet plane where the velocity is imposed. At $x/D = 5$ the GR LES is still doing a fairly good job, whereas the centerline velocity is underpredicted in the spectral LES. This is due to the earlier onset of enhanced turbulent mixing, seen earlier in Fig. 11. Beyond $x/D = 5$, both simulations underpredict the centerline velocity, and the solutions tend toward each other farther downstream.

This behavior can be seen more clearly in Fig. 16, which shows jet centerline profiles of the same quantities. The GR LES initially

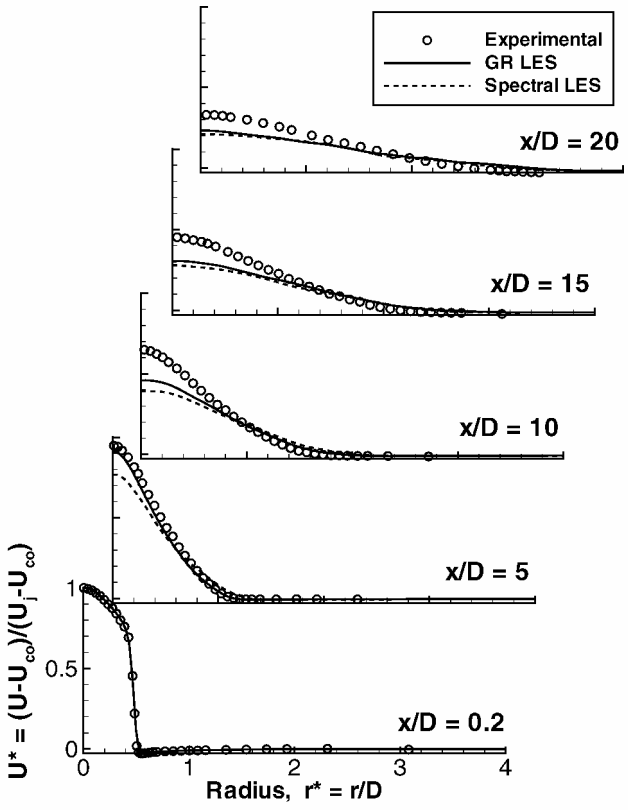

Fig. 15 Mean radial profiles of axial velocity.

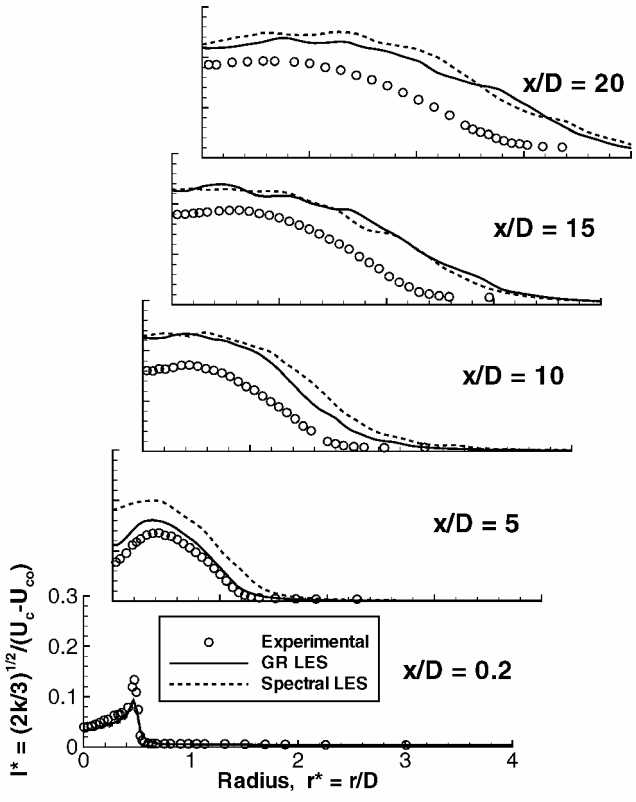

Fig. 17 Mean radial profiles of turbulence intensity.

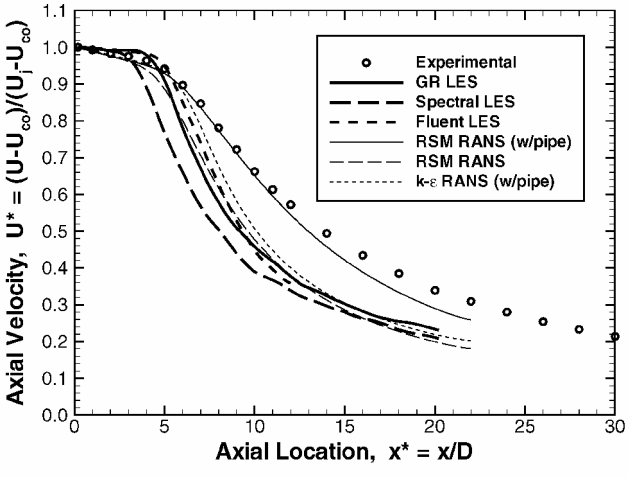

Fig. 16 Decay of mean axial velocity along jet the centerline.

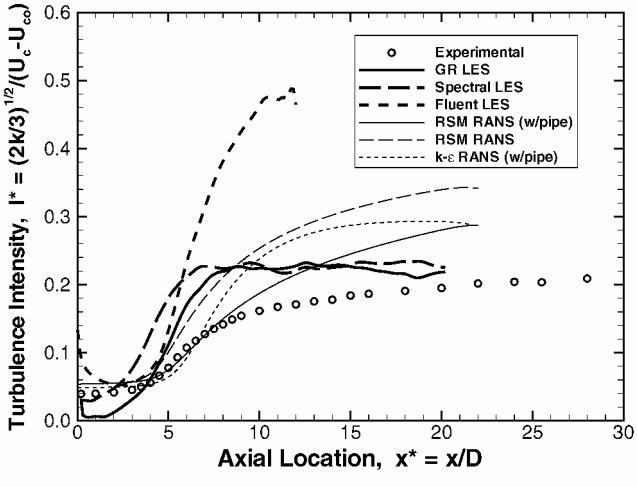

Fig. 18 Jet centerline turbulence intensity.

overpredicts the velocity until about $x/D = 5$, where the shear layers merge and turbulent mixing begins. From there, the velocity decay rate is much too rapid. The spectral LES matches the initial profile more closely, although it, too, eventually begins a rapid decay like the GR LES, starting at a location farther upstream. The Fluent LES results are also included in Fig. 16 for comparison. The results are remarkably close to that of the GR LES, which uses a similar random inlet condition treatment. Regardless of the inlet treatment, though, all LES results presented here follow a similar downstream trend.

Radial profiles of the turbulence intensity normalized by the local centerline velocity are shown in Fig. 17. Note that the intensity measured from the LES represents only the contribution from resolved scales. The Lagrangian dynamic SGS closure model used in the present work is an effective eddy-viscosity model that treats only the deviatoric portion of the SGS stress tensor. The isotropic portion of this tensor is assumed negligible and is left unmodeled,[53] effectively merging the SGS turbulent kinetic energy into the pressure where this information is lost.[54] With the original modeling assumption that this contribution is negligible, this is of minor concern in the present work.

The turbulence intensity matches the experimental profile well at $x/D = 0.2$, as it should. The slight underpredictions seen at this location are due to the explicit grid filtering removing the smallest scales of the inlet forcing. Looking farther downstream, the spectral LES initially has a larger intensity than the GR LES, but by the end of the domain the simulated intensities are almost identical to each other. Overall, the correct trends are predicted for both simulations despite a consistent overprediction at all downstream locations. Axial profiles of these same data are presented in Fig. 18, where the initial growth of turbulence intensity is seen to be too rapid for both the GR and spectral LES. This rapid growth is not just a consequence of being normalized by the underpredicted axial velocity because the unnormalized intensity also grows more rapidly than the unnormalized experimental data. After this initial growth, the

intensity for both LES appear to approach a constant magnitude. A similar trend can be seen for the experimental data.

The initial sharp drop in turbulence intensity for the Fluent LES closely matches the behavior of the GR LES. Similarly, the intensity then grows at an excessive rate and appears to start leveling off. The enhanced turbulent mixing from this overpredicted intensity explains why the centerline velocity in Fig. 16 decays slightly more rapidly than that of the GR LES.

RANS Results

The magnitude and consistency of the errors in velocity statistics described in the preceding section prompted a further investigation to ascertain whether there might be a numerical or modeling error in the LES code. Various SGS models were briefly tested, along with several numerical methods, filtering operators, and boundary condition treatments. None provided a significant change. This was one of the reasons for attempting a repeat of the simulations with the Fluent commercial CFD code. After finding a similar enhanced centerline velocity decay in this and other tests, it was decided to look elsewhere for the cause of the consistent discrepancy.

For comparison, several axisymmetric RANS simulations were performed using Fluent with various domain configurations and numerical methods. Several closure models were tested, including versions of the k–ϵ model and Reynolds stress models (RSM). All simulations used the same experimental velocity and turbulent kinetic energy profiles as were used in the LES, as well as experimental profiles of Reynolds stresses where needed. Surprisingly, all results fell along the same trends as the LES.

To continue the RANS investigation, a larger simulation was constructed that included a section of upstream pipe $80D$ in length and a section of the upstream coflow duct, as described earlier and shown in Fig. 7. Two simulations were performed with this geometry, using the realizable k–ϵ model and the RSM model. The results for these two simulations are labeled the k–ϵ RANS (w/pipe) and RSM RANS (w/pipe), respectively, in Figs. 16 and 18.

The k–ϵ simulation has the same incorrect centerline velocity trend as all earlier simulation, whereas the RSM RANS (w/pipe) was the first simulation attempted in this work that matched the experimental data reasonably closely. Admittedly, further improvements in this simulation could still be made by fine tuning the many model coefficients, but this was not the intent of the present study. What should be recognized is that the RSM RANS (w/pipe) simulation apparently includes the piece of the puzzle that was consistently missing from all earlier LES and RANS simulations.

As an additional test to isolate the problem, the exact solution of all transport variables in the RSM RANS (w/pipe) simulation was extracted at the $x/D = 0.2$ plane and used as inlet conditions for another RSM RANS simulation in a rectangular domain that did not include the upstream pipe, analogous to the LES domain configurations. The results of this simulation (labeled as RSM RANS) are shown in Figs. 16 and 18 as well. Remarkably, the centerline velocity profile did not follow that of the simulation from which the inlet conditions were extracted. The solution instead follows the same incorrect trend as all earlier simulations.

The observation can be made from these tests that, for a fully turbulent jet, it is extremely important to include the effects of Reynolds stresses as well as a portion of the upstream pipe. This is underscored by the work of Gharbi et al.[55] (also M. Amielh, personal communication, 2000), who also attempted to simulate the IRPHE jet and found similar requirements for an accurate solution.

Close observations of the RSM RANS (w/pipe) solution have indicated that the constant transport variables in the fully developed upstream pipe actually begin changing about half a jet diameter before the end of the pipe. This, along with the difference between the RSM RANS solutions with and without the pipe indicate that the numerical solutions of the jet and the pipe are critically coupled. Removal of the pipe severely damages the jet solution.

Conclusions

Two LES were performed of a fully turbulent jet using different stochastic inlet condition methodologies to approximate incoming turbulence: GR fluctuations and the WAWS spectral representation method. The GR inlet forcing, despite being used in many commercial CFD codes, was found to model a turbulent inflow poorly. The inlet fluctuations dissipated almost immediately, resulting in a jet that behaved more like a transitionally turbulent flow than a fully turbulent flow. The spectral representation inlet forcing was found to reproduce the jet near field much more accurately. Despite being completely synthetic, the spectral fluctuations allowed the flow to transition rapidly to self-sustaining turbulence. The inlet turbulence intensity did not decay at all before it began its growth to larger downstream values, as it should. The earlier growth of turbulence levels in the spectral LES lead to enhanced mixing of the jet with the coflow, resulting in a broader jet velocity profile.

Several factors precluded making conclusive statements about the accuracy of the spectral representation inlet condition methodology. Through comparisons to LES and RANS simulations performed with the Fluent commercial CFD code, it was determined that the solution in the jet and the upstream pipe are critically coupled. Removal of the pipe from the simulation severely altered the jet behavior, regardless of the accuracy of the inlet conditions. Because the pipe was not included in either LES, the measured trends were far enough from the experimental data to prevent accurate comparisons. Adding the pipe would have required converting the code to a cylindrical coordinate system to treat properly the near-wall region of the upstream pipe and was not performed in the present work.

Reynolds stresses were also found to be important to the RANS solutions. The realizable k–ϵ closure model performed poorly in the present work, whereas the RSM was capable of doing quite well. Simply imposing Reynolds stresses at the inlet of a RSM RANS that did not include the upstream pipe also lead to very poor results. It is uncertain whether inclusion of Reynolds stresses in the present spectral representation inlet forcing methodology would have made much of a difference due to the lack of an inlet pipe, although it is suspected that it would not.

Despite these issues, the spectral representation inlet forcing technique was found to have substantial merit over GR fluctuations. The intent of any inlet forcing scheme is to recreate the upstream flow as accurately as possible so that the downstream flow is allowed to develop naturally. To this end, the spectral forcing was able to generate self-sustaining inlet turbulence, whereas the random inlet forcing simply could not. It is the authors' opinion that pure random inlet forcing should not be used in unsteady simulations such as LES or DNS for the sole purpose of generating inlet turbulence. The spectral representation technique, or other stochastic field-generation techniques like it, holds promise as a simple and cost-effective way to perform fully turbulent simulations.

Acknowledgments

This work utilized Purdue University's IBM SP supercomputer and the accompanying services of Information Technology at Purdue, Purdue's central computing and communications organization. The authors thank Muriel Amielh for providing the experimental data on which this work is based and also for the many valuable correspondences throughout this project.

References

[1] Boersma, B. J., and Lele, S. K., "Large Eddy Simulation of a Mach 0.9 Turbulent Jet," AIAA Paper 99-1874, 1999.

[2] Olsson, M., and Fuchs, L., "Large Eddy Simulations of a Forced Semi-confined Circular Impinging Jet," *Physics of Fluids*, Vol. 10, 1998, pp. 476–486.

[3] Grinstein, F. F., Gutmark, E. J., Parr, T. P., Hanson-Parr, D. M., and Obeysekare, U., "Streamwise and Spanwise Vortex Interaction in an Axisymmetric Jet. A Computational and Experimental Study," *Physics of Fluids*, Vol. 8, No. 6, 1996, pp. 1515–1524.

[4] Kim, J., Moin, P., and Moser, R. D., "Turbulent Statistics in Fully Developed Turbulent Channel Flow at Low Reynolds Number," *Journal of Fluid Mechanics*, Vol. 177, 1987, pp. 133–166.

[5] Stanley, S. A., and Sarkar, S., "Influence of Nozzle Conditions and Discrete Forcing on Turbulent Planar Jets," *AIAA Journal*, Vol. 38, No. 9, 2000, pp. 1615–1623.

[6]Mi, J., Nobes, D. S., and Nathan, G. J., "Influence of Jet Exit Conditions on the Passive Scalar Field of an Axisymmetric Free Jet," *Journal of Fluid Mechanics*, Vol. 432, 2001, pp. 91–125.

[7]Pickett, L. M., and Ghandhi, J. B., "Passive Scalar Mixing in a Planar Shear Layer with Laminar and Turbulent Inlet Conditions," *Physics of Fluids*, Vol. 14, No. 3, 2002, pp. 985–998.

[8]Grinstein, F. F., Young, T. R., Gutmark, E. J., Li, G., Hsiao, G., and Mongia, H., "Flow Dynamics in a Swirl Combustor," *Journal of Turbulence*, [online journal], Vol. 3, Paper 030, URL: http://jot.iop.org [cited 26 July 2002].

[9]Ling, W., Chung, J. N., Troutt, T. R., and Crowe, C. T., "Direct Numerical Simulation of a Three-Dimensional Temporal Mixing Layer with Particle Dispersion," *Journal of Fluid Mechanics*, Vol. 358, 1998, pp. 61–85.

[10]Lund, T. S., Wu, W., and Squires, K. D., "Generation of Turbulent Inflow Data for Spatially-Developing Boundary Layer Simulation," *Journal of Computational Physics*, Vol. 140, 1998, pp. 233–258.

[11]Arnal, M., and Friedrich, R., "Large-Eddy Simulation of a Turbulent Flow with Separation," *8th Symposium on Turbulent Shear Flows*, Springer-Verlag, Berlin, 1993, pp. 169–187.

[12]Voke, P., and Yang, Z., "Numerical Study of Bypass Transition," *Physics of Fluids A*, Vol. 7, No. 9, 1995, pp. 2256–2264.

[13]Li, N., Balaras, E., and Piomelli, U., "Inflow Conditions for Large-Eddy Simulations of Mixing Layers," *Physics of Fluids*, Vol. 12, 2000, pp. 935–938.

[14]Chun, Y. M., and Sung, H. J., "Comparative Study of Inflow Conditions for Spatially Evolving Simulations," *AIAA Journal*, Vol. 35, No. 2, 1997, pp. 269–274.

[15]Bonnet, J. P., Delville, J., Druault, P., Sagaut, P., and Grohens, R., "Linear Stochastic Estimation of LES Inflow Conditions," *Proceedings of First AFOSR International Conference on DNS/LES*, Greyden Press, Columbus, OH, 1997, pp. 341–348.

[16]Devroye, L., *Non-Uniform Random Variate Generation*, Springer-Verlag, New York, 1986, Chap. 9.

[17]Swami, A., Giannakis, G., and Shamsunder, S., "Multichannel ARMA Processes," *IEEE Transactions on Signal Processing*, Vol. 42, No. 4, 1994, pp. 898–913.

[18]Mignolet, M. P., and Spanos, P. D., "Recursive Simulation of Stationary Multivariate Random Processes—Part I," *Transactions of the American Society of Mechanical Engineers*, Vol. 54, 1987, pp. 674–680.

[19]Spanos, P. D., and Mignolet, M. P., "Recursive Simulation of Stationary Multivariate Random Processes—Part II, *Transactions of the American Society of Mechanical Engineers*, Vol. 54, 1987, pp. 681–687.

[20]Shinozuka, M., "Simulation of Multivariate and Multidimensional Random Processes," *Journal of the Acoustical Society of America*, Vol. 49, No. 1, 1971, pp. 357–368.

[21]Shinozuka, M., and Jan, C. M., "Digital Simulation of Random Processes and Its Application," *Journal of Sound and Vibration*, Vol. 25, No. 1, 1972, pp. 111–128.

[22]Schuëller, G. I., "A State-of-the-Art Report on Computational Stochastic Mechanics," *Probabilistic Engineering Mechanics*, Vol. 12, No. 4, 1997, pp. 197–321.

[23]Deodatis, G., "Simulation of Ergodic Multivariate Stochastic Processes," *Journal of Engineering Mechanics*, Vol. 122, No. 8, 1996, pp. 778–787.

[24]Yang, J. N., "Simulation of Random Envelope Processes," *Journal of Sound and Vibration*, Vol. 21, No. 1, 1972, pp. 73–85.

[25]Shinozuka, M., and Deodatis, G., "Simulation of Multi-Dimensional Gaussian Stochastic Fields by Spectral Representation," *Applied Mechanics Review*, Vol. 49, No. 1, 1996, pp. 29–53.

[26]Deodatis, G., "Non-Stationary Stochastic Vector Processes: Seismic Ground Motion Applications," *Probabilistic Engineering Mechanics*, Vol. 11, 1996, pp. 149–168.

[27]Yamazaki, F., and Shinozuka, M., "Digital Generation of Non-Gaussian Stochastic Fields," *Journal of Engineering Mechanics*, Vol. 114, 1988, pp. 1183–1197.

[28]Kondo, K., Murakami, S., and Mochida, A., "Generation of Velocity Fluctuations for Inflow Boundary Condition of LES," *Journal of Wind Engineering*, Vols. 67 and 68, 1997, pp. 51–64.

[29]Le, H., and Moin, P., "Direct Numerical Simulation of Turbulent Flow over a Backward-Facing Step," Dept. of Mechanical Engineering, Rept. TF-58, Stanford Univ., Stanford, CA, Dec. 1994.

[30]Amielh, M., Djeridane, T., Anselmet, F., and Fulachier, L., "Velocity Near-Field of Variable Density Turbulent Jets," *International Journal of Heat and Mass Transfer*, Vol. 39, No. 10, 1996, pp. 2149–2164.

[31]Djeridane, T., Amielh, M., Anselmet, F., and Fulachier, L., "Velocity Turbulence Properties in the Near-Field Region of Axisymmetric Variable Density Jets," *Physics of Fluids*, Vol. 8, No. 6, 1996, pp. 1614–1630.

[32]DesJardin, P. E., and Frankel, S. H., "Large Eddy Simulation of a Nonpremixed Reacting Jet: Application and Assessment of Subgrid-Scale Combustion Models," *Physics of Fluids*, Vol. 10, No. 9, 1998, pp. 2298–2314.

[33]Lele, S. K., "Compact Finite Difference Schemes with Spectral-Like Resolution," *Journal of Computational Physics*, Vol. 103, 1992, pp. 16–42.

[34]Ghosal, S., "An Analysis of Numerical Errors in Large-Eddy Simulations of Turbulence," *Journal of Computational Physics*, Vol. 125, 1996, pp. 187–206.

[35]Lund, T. S., and Kaltenbach, H.-J., *Experiments with Explicit Filtering for LES Using a Finite-Difference Method*, Annual Research Briefs, Center for Turbulence Research, NASA Ames Research Center/Stanford Univ., Stanford, CA, 1995, pp. 91–105.

[36]Carpenter, M. H., Gottlieb, D., and Abarbanel, S., "The Stability of Numerical Boundary Treatments for Compact High-Order Finite-Difference Schemes," *Journal of Computational Physics*, Vol. 108, 1993, pp. 272–295.

[37]Carpenter, M. H., Gottlieb, D., and Abarbanel, S., "Time-Stable Boundary Conditions for Finite-Difference Schemes Solving Hyperbolic Systems: Methodology and Application to High-Order Compact Schemes," *Journal of Computational Physics*, Vol. 111, 1994, pp. 220–236.

[38]Moin, P., "Progress in Large Eddy Simulations of Turbulent Flows," AIAA Paper 97-0749, Jan. 1997.

[39]Germano, M., "Turbulence: The Filtering Approach," *Journal of Fluid Mechanics*, Vol. 238, 1992, pp. 325–336.

[40]Ghosal, S., Lund, T. S., Moin, P., and Akselvoll, K., "A Dynamic Localization Model for Large-Eddy Simulation of Turbulent Flow," *Journal of Fluid Mechanics*, Vol. 286, 1995, pp. 229–255.

[41]Germano, M., Piomelli, U., Moin, P., and Cabot, W. H., "A Dynamic Subgrid-Scale Eddy Viscosity Model," *Physics of Fluids A*, Vol. 3, No. 7, 1991, pp. 1760–1765.

[42]Meneveau, C., Lund, T. S., and Cabot, W. H., "A Lagrangian Dynamic Subgrid-Scale Model of Turbulence," *Journal of Fluid Mechanics*, Vol. 319, 1996, pp. 353–385.

[43]Poinsot, T. J., and Lele, S. K., "Boundary Conditions for Direct Simulations of Compressible Viscous Flows," *Journal of Computational Physics*, Vol. 101, 1992, pp. 104–129.

[44]Veers, P. S., "Three-Dimensional Wind Simulation," Sandia National Labs., TR SAND88-0152, Albuquerque, NM, March 1988.

[45]Winkelaar, D., "Fast Three-Dimensional Wind Simulation and the Prediction of Stochastic Blade Loads," *Tenth ASME Wind Energy Symposium*, Vol. SED 11, American Society of Mechanical Engineers, Fairfield, NJ, 1991, pp. 5–14.

[46]Bremhorst, K., and Walker, T. B., "Spectral Measurements of Turbulent Momentum Transfer in a Fully Developed Pipe Flow," *Journal of Fluid Mechanics*, Vol. 61, 1973, pp. 173–186.

[47]Mattor, N., Williams, T. J., and Hewett, D. W., "Algorithm for Solving Tridiagonal Matrix Problems in Parallel," *Parallel Computing*, Vol. 21, 1995, pp. 1769–1782.

[48]Visbal, M. R., and Rizzetta, D. P., "Large-Eddy Simulation on Curvilinear Grids Using Compact Differencing and Filtering Schemes," *Journal of Fluids Engineering*, Vol. 124, 2002, pp. 836–847.

[49]Pope, S. B., *Turbulent Flows*, Cambridge Univ. Press, Cambridge, England, U.K., 2000.

[50]Branley, N., and Jones, W. P., "Large Eddy Simulation of a Turbulent Non-Premixed Flame," *Combustion and Flame*, Vol. 127, 2001, pp. 1914–1934.

[51]Jeong, J., and Hussain, F., "On the Identification of a Vortex," *Journal of Fluid Mechanics*, Vol. 285, 1995, pp. 69–94.

[52]Zaman, K. B. M. Q., and Hussain, A. K. M. F., "Vortex Pairing in a Circular Jet Under Controlled Excitation: Part I. General Jet Response," *Journal of Fluid Mechanics*, Vol. 101, 1980, pp. 440–491.

[53]Erlebacher, G., Hussaini, M. Y., Speziale, C. G., and Zang, T. A., "Toward the Large Eddy Simulation of Compressible Turbulent Flows," *Journal of Fluid Mechanics*, Vol. 238, 1992, pp. 155–185.

[54]Winckelmans, G. S., Jeanmart, H., and Carati, K., "On the Comparison of Turbulence Intensities from Large-Eddy Simulation with Those from Experiment or Direct Numerical Simulation," *Physics of Fluids*, Vol. 14, No. 5, 2002, pp. 1809–1811.

[55]Gharbi, A., Ruffin, E., Anselmet, F., and Schiestel, R., "Numerical Modelling of Variable Density Turbulent Jets," *International Journal of Heat and Mass Transfer*, Vol. 39, 1996, pp. 1865–1882.

P. Givi
Associate Editor